

ADVANCED ENERGY MATERIALS

Supporting Information

for *Adv. Energy Mater.*, DOI: 10.1002/aenm.201803536

Highly Efficient Solar-Driven Carbon Dioxide Reduction on Molybdenum Disulfide Catalyst Using Choline Chloride-Based Electrolyte

Mohammad Asadi, Mohammad Hossein Motevaselian, Alireza Moradzadeh, Leily Majidi, Mohammadreza Esmaeilirad, Tao Victor Sun, Cong Liu, Rumki Bose, Pedram Abbasi, Peter Zapol, Amid P. Khodadoust, Larry A. Curtiss, Narayana R. Aluru, and Amin Salehi-Khojin**

Supporting Information

Highly Efficient Solar-driven Carbon Dioxide Reduction on Molybdenum Disulfide Catalyst using Choline Chloride based Electrolyte

Mohammad Asadi^{1†}, Mohammad Hossein Motevaselian^{2†}, Alireza Moradzadeh², Leily Majidi³, Mohammadreza Esmaeilirad¹, Tao Victor Sun², Cong Liu⁴, Rumki Bose³, Pedram Abbas³, Peter Zapol⁵, Amid P. Khodadoust⁶, Larry A. Curtiss⁵, Narayana R. Aluru^{2*}, Amin Salehi-Khojin^{3*}

¹Department of Chemical and Biological Engineering, Illinois Institute of Technology, Chicago, IL, 60616, USA.

²Department of Mechanical Science and Engineering, Beckman Institute for Advanced Science and Technology, University of Illinois at Urbana-Champaign, Urbana, IL, 61801, USA.

³Department of Mechanical and Industrial Engineering, University of Illinois at Chicago, Chicago, IL, 60607, USA.

⁴Chemical Sciences and Engineering Division, Argonne National Laboratory, Argonne, IL, 60439, USA.

⁵Materials Science Division, Argonne National Laboratory, Argonne, IL, 60439, USA.

⁶Department of Civil and Materials Engineering, University of Illinois at Chicago, Chicago, IL, 60607, USA.

[†] These authors equally contributed to this work.

[*] Corresponding authors, salehikh@uic.edu, aluru@illinois.edu

Table of Contents:

S1. MoS₂ characterization

S2. Three-electrode electrochemical setup

S3. Product characterization of three-electrode electrochemical setup

S4. Electrochemical impedance spectroscopy (EIS)

S5. Flow cell for continuous CO₂ reduction reaction

S6. Chronoamperometry results of flow cell experiments

S7. Resistance measurement of flow cell

S8. Product analysis of flow cell experiments

S9. Stability of the electrolyte

S10. K⁺ and H⁺ concentrations in flow cell experiments

S11. Performance of the TJ-PV cell at different sun illuminations

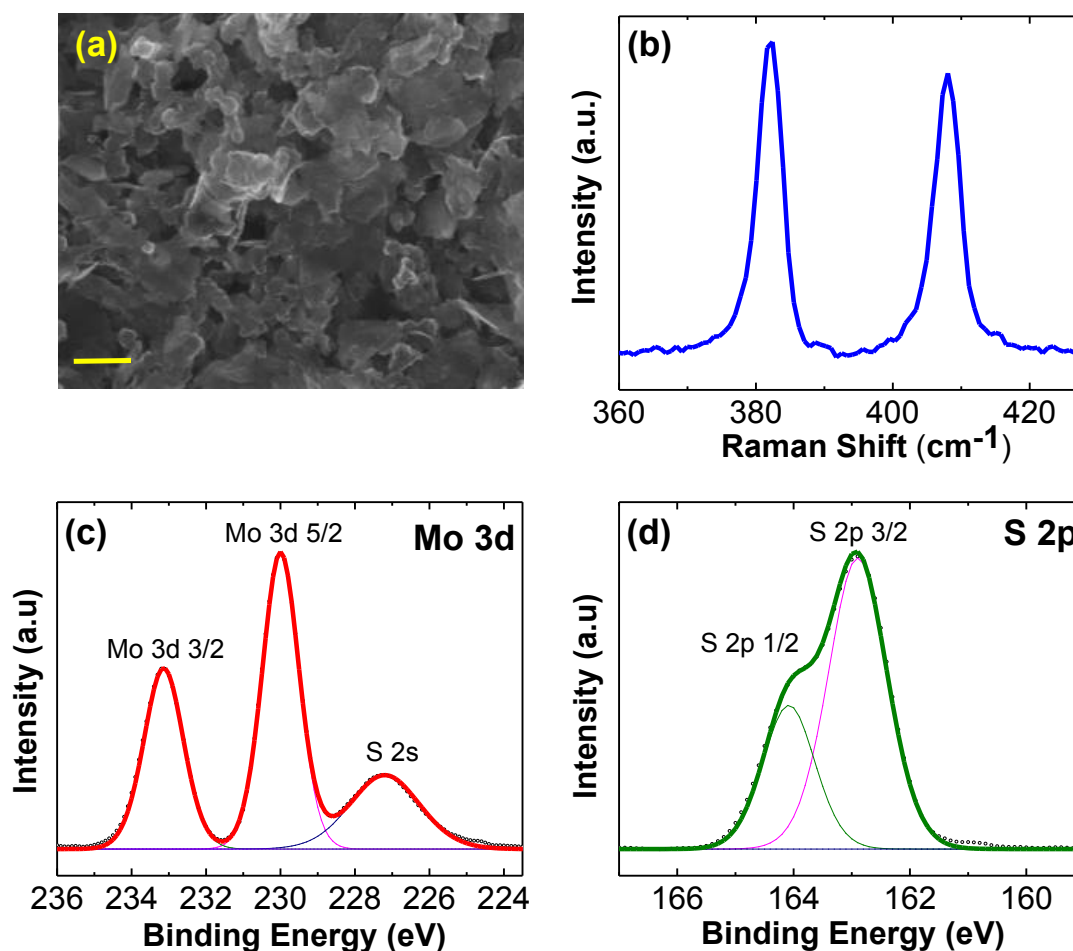
S12. Solar to fuel efficiency of the solar-driven flow cell

S13. Density functional theory (DFT) calculation

S14. Classical molecular dynamics simulation (MD)

S1. MoS₂ characterization

Supporting Figure 1a shows the SEM image acquired by an acceleration voltage (EHT) of 10 kV in lens magnification of 20 kX. Supporting Figure 1b shows the Raman spectrum of MoS₂ NFs. Two main Raman peaks of MoS₂ are observed at 382.24 and 408.09 cm⁻¹ which correspond to E_{2g}¹ and A_{1g} vibrational modes, respectively.^[1] Supporting Figures 1c-d show the XPS spectra of MoS₂ catalyst. Mo 3d spectrum in Supporting Figure 1c includes two main peaks at 229.9 and 233.1 eV representing Mo 3d_{5/2} and Mo 3d_{3/2} core level peaks. Another peak is observed at 227.17 eV indicating S 2s core level peak. Supporting Figure 1d indicates two distinguished S 2p_{3/2} and S 2p_{1/2} peaks located at 162.8 and 164.0 eV.^[2]



Supporting Figure 1. (a) SEM image of MoS₂ NFs coated on GDL. Scale bar is 200 nm. (b) Raman spectrum of MoS₂ NFs (c) XPS spectrum of Mo 3d core level peaks. (d) XPS spectrum of S 2p core level peaks.

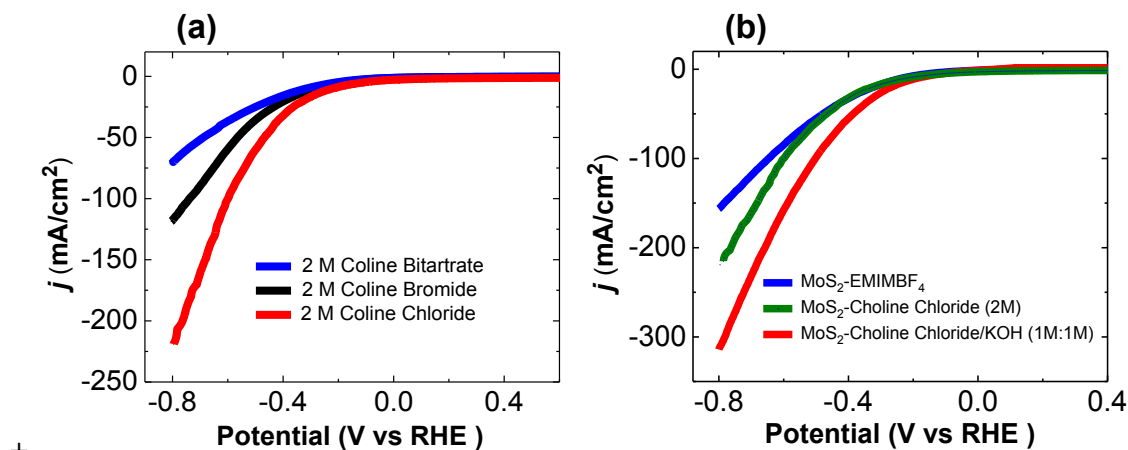
S2. Three-electrode electrochemical setup

For all electrochemical experiments, a two-compartment three-electrode electrochemical cell was used to perform carbon dioxide (CO₂) reduction reaction. The synthesized MoS₂ NFs^[3] coated on glassy carbon (GC) substrate, Platinum (Pt) gauze 52 mesh (Alfa Aesar) and Ag/AgCl (BASi) were used as working, counter and reference electrodes, respectively. Pure CO₂ gas (99.99%, Praxair) was bubbled into different prepared electrolytes for 30 minutes before each experiment.

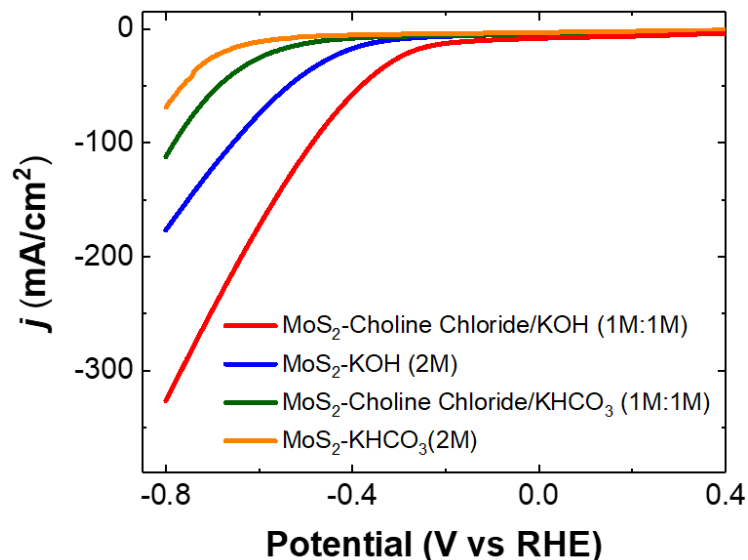
All potentials were converted to the Reversible Hydrogen Electrode (RHE) using Equation S1 considering the pH of the solution.

$$\text{Potential in RHE} = \text{Applied potential vs Ag/AgCl} + 0.197 \text{ V} + 0.0592 \times \text{pH} \quad (\text{Equation S1})$$

The pH of solutions was constantly measured during the experiments. The cell was connected to the potentiostat (CH Instruments) for the electrolysis experiments. The polarization curves (j - V) were obtained by sweeping the potential between +0.4 and -0.8 V vs. RHE at 50 mV/s. The LSV experiment results are shown in Supporting Figure 2.

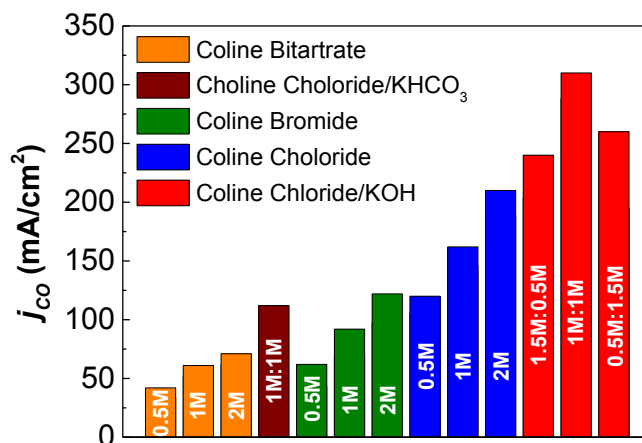


Supporting Figure 2. Current density of MoS₂ in. (a) 2M of different amine based electrolytes (b) in 2M choline chloride, 50:50 vol% EMIMBF₄/DI water and 1M choline chloride/1M KOH hybrid electrolyte.



Supporting Figure 3. LSV results of MoS₂ NFs in different electrolytes.

Supporting Figure 4 shows the current density of MoS₂ NFs cathode at electrolytes with different salt concentrations at the potential of -0.8V. The results indicate that the electrolyte with the ratio of 1M choline chloride and 1M KOH shows the highest current density among the tested electrolytes.

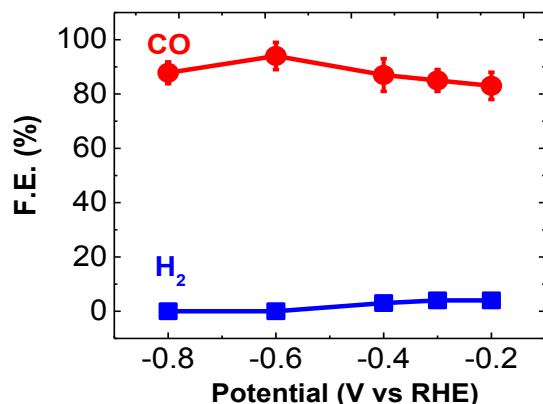


Supporting Figure 4: Current density for different electrolytes with different salt concentrations at the potential of -0.8V vs RHE.

S3. Product characterization of three-electrode electrochemical setup

Product characterization was carried out using an SRI 8610C GC system equipped with 72 ×18 inches S.S molecular sieve-packed column and a thermal conductivity detector (TCD). Ultra-high purity helium and nitrogen gasses (99.99% purchased from Praxair) were used as the carrier gas for CO and H₂ detection, respectively. For product characterization, chronoamperometry measurements were performed for the desired time (~15 mins) and 1 mL samples were taken out from the dead volume of the cell using a lock-in syringe (Hamilton) and injected into the Gas chromatography system under identical conditions. Faradic efficiency measurements were calculated using Equation S2.

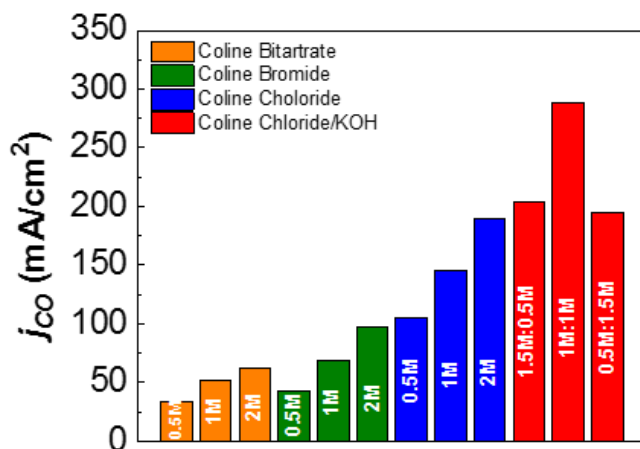
$$FE\% = \frac{\text{moles of product (measured by GC)}}{j \text{ (mA/cm}^2\text{)} \times t \text{ (s)} / nF} \times 100 \quad (\text{Equation S2})$$



Supporting Figure 5. Faradaic efficiency (F.E.) of MoS₂ NFs in the hybrid electrolyte of choline chloride/KOH (1:1 M).

Faradaic efficiency (F.E.) calculations indicate the formation of CO as the dominant products for MoS₂ catalyst in the hybrid electrolyte of choline chloride/KOH (1:1 M) (Supporting Figure 5). The overall F.E. of 90%±5 was calculated at potential window of -0.2 to -0.8 V vs. RHE for our studied catalysts systems.

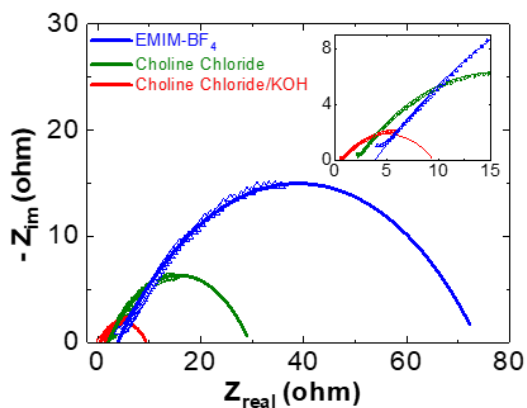
Supporting Figure 6 shows the CO partial current density at the cell potential of -0.8V for different electrolytes. Results indicate that the hybrid electrolyte of choline chloride (1:1) shows the highest partial CO formation current density among tested electrolytes.



Supporting Figure 6: Calculated CO partial current density for different electrolytes with different concentrations at the potential of -0.8V vs. RHE.

S4. Electrochemical impedance spectroscopy (EIS)

EIS experiments were performed inside a two-compartment three-electrode electrochemical cell comprised of MoS₂ as the cathode, platinum (Pt) gauze 52 mesh (purchased via Alfa Aesar) as the anode and Ag/AgCl (3M KCl, purchased from BASi) as the working electrode.

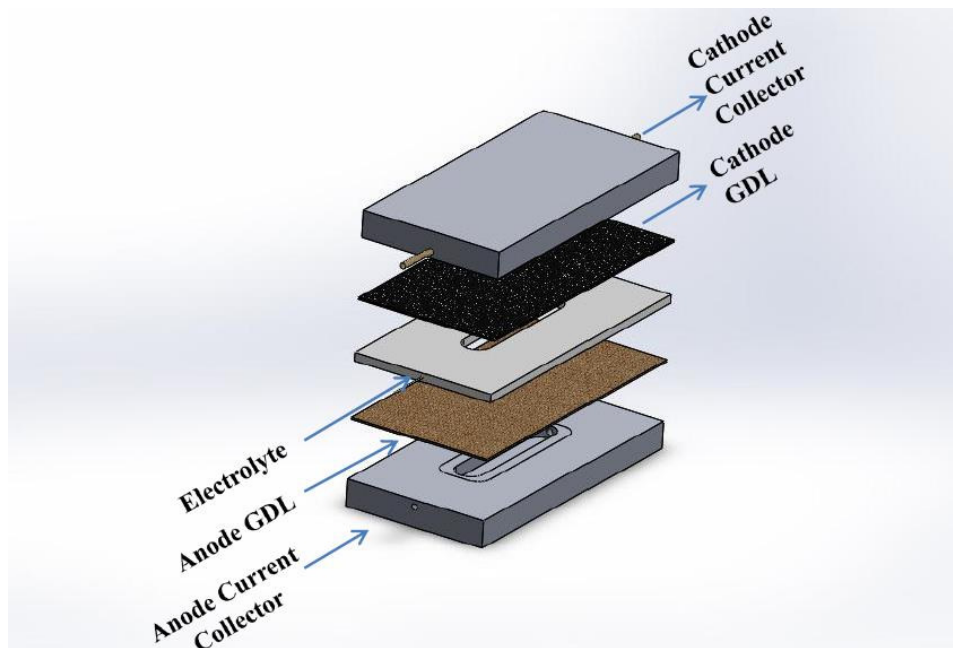


Supporting Figure 7. Electrochemical impedance spectroscopy (EIS) measurement for MoS₂ NFs inside different electrolytes.

The Nyquist plot for CO₂ reduction at the cell potential of -2.0V was recorded at a small (10 mV) AC voltage amplitude (to avoid the nonlinearity) and over a frequency range of 10 to 10⁵ Hz using a Voltalab PGZ100 potentiostat.^[4,5] Supporting Figure 7 shows the obtained Nyquist plots and fitted curves for MoS₂ in different electrolytes at the cell potential of -2.0 V.

S5. Flow cell for continuous CO₂ reduction reaction

The electrocatalytic activity of MoS₂ catalyst as the cathode, Iridium oxide nanoparticles (IrO₂ NPs) as the anode side and the electrolyte with the ratio of 1M choline chloride and 1M KOH were studied in a flow cell (Supporting Figure 8).



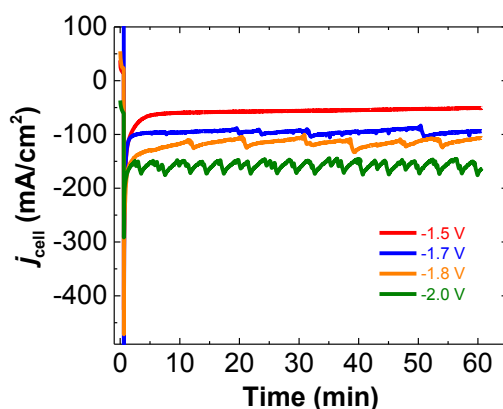
Supporting Figure 8. A schematic of flow cell for continuous CO₂ reduction reaction.

The cathode and the anode were coated on GDEs with their respective catalysts. 10 mg of MoS₂ nanoflakes (100 nm) was mixed in a solution of 0.6 mL isopropanol, 0.6 mL DI water, and 0.01 mL of 1100 EW 5% Nafion solution (DuPont).^[6] The solution was then sonicated for 5 minutes before being applied into an area of 1.25 cm² on the GDE using a paintbrush. The same procedure was adapted for the anode catalyst, except that 10 mg of IrO₂ nanoparticles (50 nm, Alfa Aesar) were utilized in place of the MoS₂. The cathode and anode were in contact with their respective aluminum current collectors. These also served as gas channels to flow CO₂ into the reactor at the cathode, and to flow O₂ out from the reactor at the anode. A mass flow controller

(Sierra Instrument, model SmartTrack 50) connected to the top gas channel through a 2 mm dia. stainless steel tube, was used to supply the CO₂ at 5 mL min⁻¹ flow rate.

S6. Chronoamperometry results of flow cell experiments

The chronoamperometry (CA) mode was used to study the performance of the flow cell reactor by applying different cell potentials (potential difference between cathode and anode) and reading the current at the same time. The cathode potentials were also monitored during the experiment. The CA results of the flow cell at different cell potentials (-1.5 to -2.0 V) are presented in Supporting Figure 9. Several CA experiments were performed by the potentiostat to analyze the products.

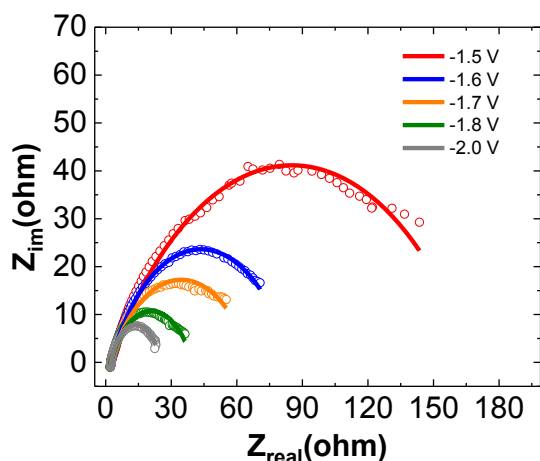


Supporting Figure 9. CA results of the flow cell at different cell potentials.

S7. Resistance measurement of flow cell

To calculate the internal cell resistances during the electrochemical process we performed EIS experiment of the flow cell at different applied potentials such as -1.5, -1.6, -1.7, -1.8, and -2.0 V. The Nyquist plot for CO₂ reduction at different cell potentials were recorded at a small (10 mV) AC voltage amplitude (to avoid the nonlinearity) and over a frequency range of 1 to 10⁵ Hz using a Voltalab PGZ100 potentiostat. Supporting Figure 10 shows the obtained Nyquist plots and fitted curves at the different cell potentials. As shown in the figure the internal resistances of

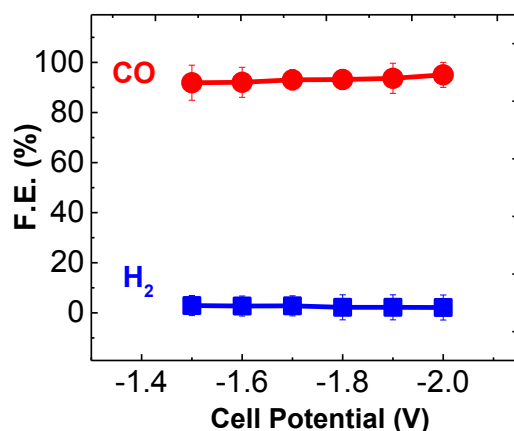
180, 100, 75, 45 and 25 ohm, respectively, were obtained at cell potentials of -1.5, -1.6, -1.7, -1.8, and -2.0 V. These results clearly indicate minor potential drop due to the internal resistance in the flow cell.



Supporting Figure 10. EIS experiment of the flow cell at different cell potentials.

S8. Product Analysis of flow cell experiments

The exit of gas channel was connected to the GC for gas detection through an external 3-port valve (provided by SRI). The product stream analysis as shown in Supporting Figure 11 indicates that the CO is the main product at different applied potentials (-1.5 to -2V) with an overall F.E. of $93\pm 5\%$. The F.E. of the reactor at different applied potentials was measured by using Equation S2. As shown in Supporting Figure 11 the average CO F.E. of $\sim 91\%$ and H_2 F.E. of $\sim 2\%$ were obtained at the different cell potentials.



Supporting Figure 11. F.E. results of flow cell at different applied cell potentials (-1.5 to -2.0 V). Error bars show the standard deviation of three measurements.

S9. Stability of the electrolyte

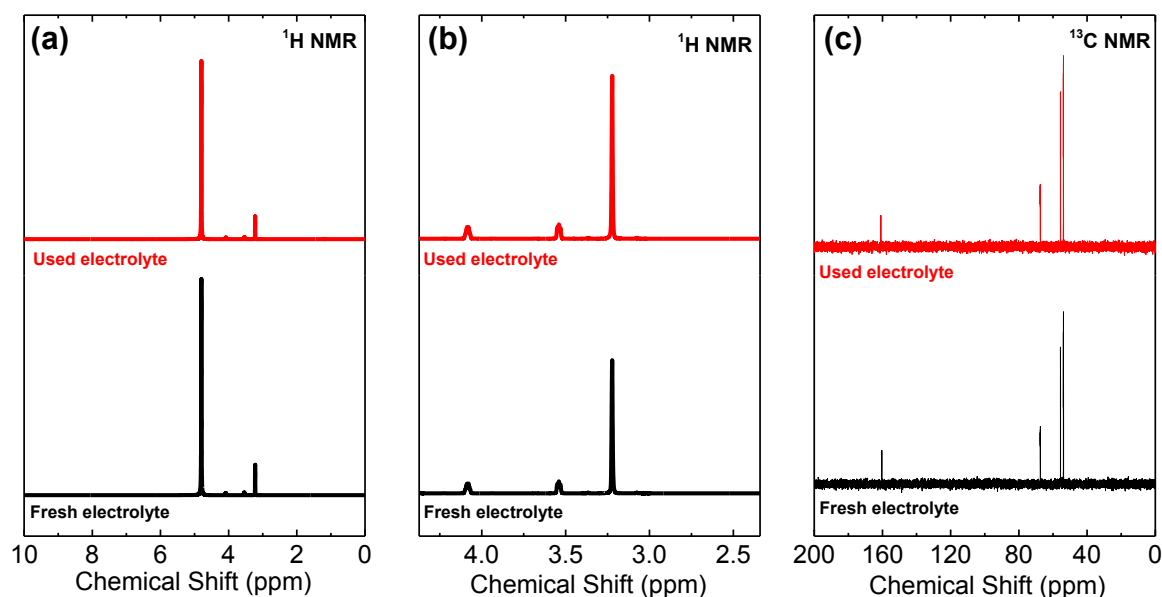
To examine the stability of electrolyte nuclear magnetic resonance (NMR) experiments of the fresh and used electrolytes (KOH: choline chloride = 1M:1M) was performed. To collect the used sample, the flow cell experiment was performed by running at -2.0 V potential for at least 40 minutes and circulating the electrolyte in the continuous process during this time. The fresh and used electrolyte samples were then collected for the NMR experiments. The NMR samples were prepared by mixing 0.1 mL electrolyte and 0.9 mL D₂O. 5 mm NMR glass tubes were used to contain the samples. ¹H NMR experiment was carried out with a Bruker Advance III 500 MHz system equipped with DCH cryoprobe at Integrated Molecular Structure Education and Research Center (IMSERC) at Northwestern University, to characterize the stability of the electrolyte. The experiments were carried out at 298 K.

Supporting Figure 12 shows ¹H NMR and ¹³C NMR spectra of fresh electrolyte purged with CO₂ and used electrolyte, respectively. The results in Supporting Figure 12a-b show peak at 3.22 ppm which corresponds to -CH₃ groups attached to nitrogen for both fresh and used electrolytes. The peaks were integrated and integration values were calculated as 9.2 and 9.1 for both fresh and used electrolytes, respectively, which corresponded to 9 identical protons. Similarly, peaks at 3.53 and 4.08 ppm represent -CH₂ group next to nitrogen and oxygen, respectively. These peak areas are in the range of 1.9 - 2.0 correspond to two protons attached to each carbon. Solvent peak (H₂O+D₂O) overlaps with -OH peak and appears at a chemical shift of 4.80 ppm. Similar peak areas and chemical shift of -CH₂ and -CH₃ peaks for both fresh and used electrolytes

confirm no change in the choline chloride structure and thus verify high stability under applied potential.

Moreover, the results for ^{13}C NMR is shown in Supporting Figure 12c. In both spectra three distinguished peaks of choline chloride were observed. The peak located at 53.88 ppm correspond to $-\text{CH}_3$ group where the $-\text{CH}_2$ group peaks appeared at 55.59 and 67.41 ppm. In both spectra, one last peak appeared at 160.9 ppm which represents bicarbonate (HCO_3^-) group.^[7-9]

Comparison between the two NMR spectra verifies the stability of prepared electrolyte.

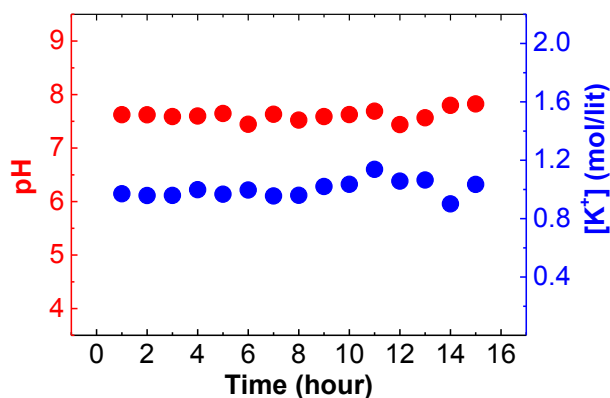


Supporting Figure 12. Nuclear Magnetic Resonance (NMR) results of fresh and used electrolytes: (a) ^1H NMR (b) Magnified three main peaks of ^1H spectra and (c) ^{13}C NMR

S10. K^+ and H^+ concentrations in flow cell experiments

The analysis of potassium (K^+) in solution was carried out using flame atomic absorption spectroscopy (FAAS) with a PerkinElmer Analyst 800 (PerkinElmer, Shelton, CT). The concentration of potassium in aqueous solution was determined using a Lumina Hollow Cathode Lamp (HCL) by FAAS with an acetylene-air mixture. The lower limit of quantitation for

potassium analysis was 0.25 mg L^{-1} using a multi-point calibration from 0.25 mg L^{-1} to 2 mg L^{-1} . The pH of the solution was also measured by using Orion Thermo-Fisher A111 pH meter. The concentration of K^+ and H^+ of the electrolyte were measured at 30 minute time intervals during a 15 hour continuous process (Supporting Figure 13).

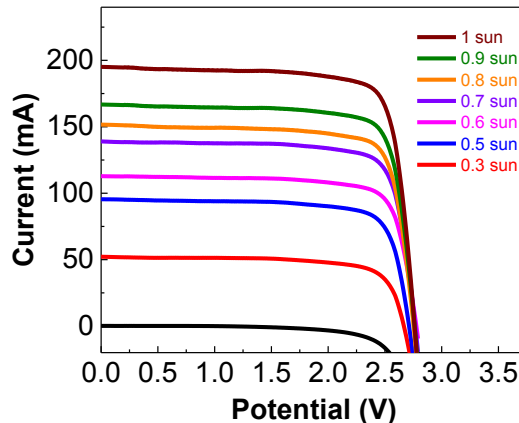


Supporting Figure 13. K^+ and H^+ concentrations during a 15 hour continuous process.

The results indicate that concentrations of both cations remain fairly constant confirming the stability of electrolyte as well as a charge neutrality during the electrochemical process.

S11. Performance of the TJ-PV cell at different sun illuminations

For the standalone self-operating process, the reactor was connected to a triple junction photovoltaic (TJ-PV) solar cell (Supporting Figure 14) in order to power the reactor with solar energy. A DC/DC regulator was used to adjust the potential generated by the PV cell to the value required by the reactor (-1.5 to -2.0V). The PV cell was characterized by connecting the PV cell to the potentiostat. Supporting Figure 14 shows i - V curves of the cell obtained at different sun illuminations. The results show that at one sun illumination the TJ-PV cell generates a photocurrent of 182.5 mA suggesting a total efficiency of 28.5% that is 2.26% less than maximum TJ-PV cell efficiency (29.1%).



Supporting Figure 14. PV cell characterization at different sun illuminations.

S12. Solar to fuel efficiency of the solar-driven flow cell

The solar to fuel efficiency of the flow cell was calculated by using Equation S3:

$$\text{SFE} = \text{TJ-PV cell efficiency} \times \text{flow cell efficiency (Equation S3)}$$

Where the TJ-PV cell efficiency is 28.5% and the flow cell efficiency is calculated by using Equation S4 as follow:

$$\text{Flow cell efficiency} = \frac{F.E. \times 1.34(V)}{\text{cell potential}(V)} \quad (\text{Equation S4})$$

The flow cell efficiency was also calculated at different cell potentials and its corresponding F.E (Figure 2b of the main manuscript).

S13. Density Functional Theory (DFT) calculation

S13.1. Computational setup and details

The computational set up for density functional theory (DFT) calculations and ab-initio molecular dynamics (AIMD) simulations have been stated in the Method section of the main text. Here we present more details.

AIMD simulations were performed to investigate the interactions of various species in the hybrid choline chloride/KOH system. First, in a system with all the molecular/ionic species (including choline cations, Cl^- anions, K^+ cations, OH^- anions, CO_2 molecules and H_2O molecules), we

observe only the phenomenon of CO₂ binding with OH⁻ within the AIMD simulation time scale (several picoseconds). In order to further explore the reactions between CO₂ molecules and OH⁻ ions, we performed AIMD simulations with 51 H₂O molecules, 1 CO₂ molecule and 1 OH⁻ ion in a box of size 10.0 Å × 16.0 Å × 10.0 Å. One extra electron was added to the system to compensate the charge carried by the OH⁻ ion. The resultant snapshots of the trajectory are shown in Figure 5a in the main text.

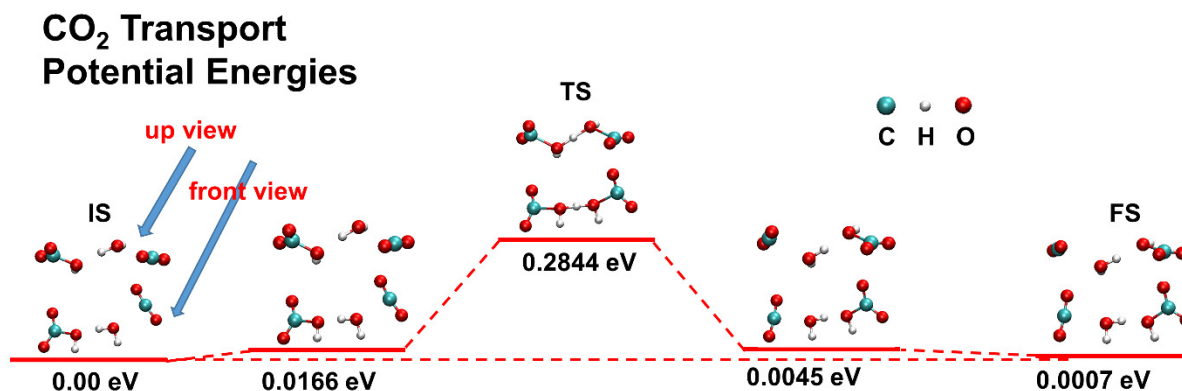
Climbing image nudged elastic band (CI-NEB) method^[10,11] was employed to investigate the CO₂ exchange procedure and the MoS₂ surface catalytic effects. For the CO₂ exchange step, 1 CO₂ molecule, 1 H₂O molecule, and 1 HCO₃⁻ ion were centered in a box of 25.0 Å × 25.0 Å × 25.0 Å. One extra electron was added to the system to compensate for the charge carried by the HCO₃⁻ ion. The initial state (IS) and the final state (FS) were obtained by optimizing the structures in which the CO₂ and the HCO₃⁻ ion got exchanged. CI-NEB simulations were carried out to obtain the minimum energy path (MEP) and the transition state (TS) energy.

For MoS₂ NF catalytic processes, single-layer nanoribbons (15 Mo atoms and 30 S atoms) with zigzag Mo edges were used. K atoms were added to the system based on the density distribution obtained by the classical MD simulations (Figure 4 in the main text). A 10 Å vacuum space was applied both on top of Mo edges and perpendicular to the MoS₂ nanoribbon planes to avoid the nonphysical interactions between images. One extra electron was added into the systems to mimic the electrochemical processes. The *COOH formation and *CO formation steps were calculated with CI-NEB methods to obtain the MEP and TS. During the structural optimization, the MoS₂ nanoribbons and the surrounding K atoms were fixed. Only the C, H and O atoms of the adsorbates were allowed to move.

The solvation corrections to the total potential energies for the above processes were calculated by adding H₂O solutions. The free energy corrections at 298 K were calculated based on the vibrational frequencies of the specific species. The vibrational frequencies were obtained with finite displacement method within the harmonic approximation. The zero-point energies (ZPEs), enthalpy (H) and entropy (-TS) contributions to the free energy corrections were calculated from these frequencies with standard methods.^[12]

S13.2. CO₂ exchange step

The complete potential energy landscape of different stages for CO₂ exchange process are presented in Supporting Figure 15. The CO₂ equilibrium exchange process is achieved by the exchange between CO₂ and HCO₃⁻ ion, with one extra H₂O molecule participating. This is similar to the mechanism proposed by Dunwell et al.^[13] This mechanism allows CO₂ to hop between HCO₃⁻ ions in solution so that rapid CO₂ diffusion could be realized. A potential energy barrier of 0.2844 eV is shown by the transition state.

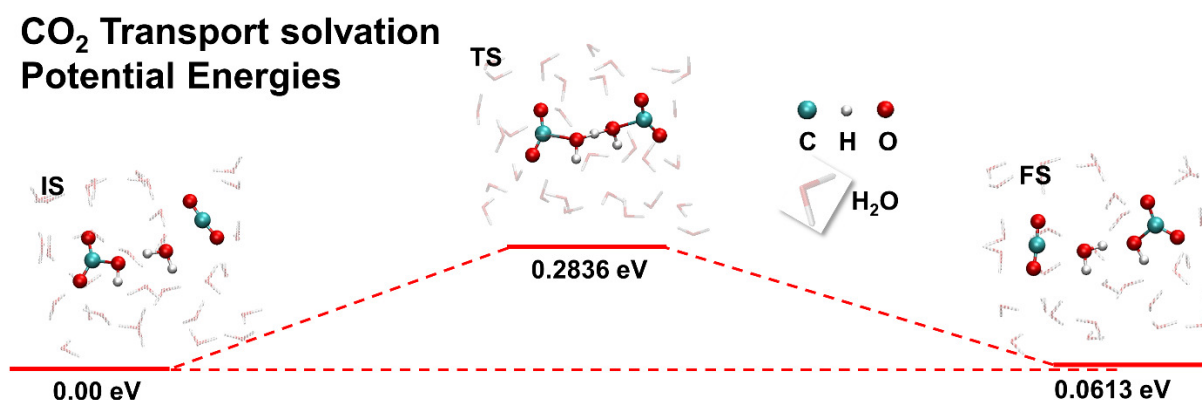


Supporting Figure 15: Potential Energy landscape of CO₂ exchange through the equilibrium process of dissolved CO₂ and the HCO₃⁻ ion. One H₂O participates in the exchange process. The initial state (IS), transition state (TS) and the final state (FS) are shown.

Bader charge analysis^[14-17] was applied to the initial state configuration to study the charge distribution for different groups. The results show that in the initial state, the H₂O group and the CO₂ group carry 8.026498 and 16.031577 electrons, respectively, showing they are charge-

neutral molecules. The HCO_3^- group takes 23.941926 electrons, which is nearly 1 more electron than its charge-neutral state, indicating that we have a HCO_3^- ion in the system. This also confirms that adding one extra electron into the system and performing structural relaxation would be able to recover the charge-carrying ions in the system.

Solvation effect corrections for the initial, transition and final states of CO_2 exchange step were calculated. During the solvation process, 32 water molecules were added around the species, and structural relaxations were performed. The originally optimized H_2O , CO_2 and HCO_3^- species were kept fixed and only the added H_2O molecules around the original species could move. The optimal solvation structures were obtained and the energy differences were recorded. The potential energy landscape with the corresponding relaxed configurations for the initial, transition and final states after solvation is shown in Supporting Figure 16. From the energy values, we could see the solvation effect corrections are rather small for all the states.



Supporting Figure 16: Potential Energy landscape of CO_2 exchange through the equilibrium process of dissolved CO_2 and the HCO_3^- ion, with explicit solvation. Only the initial state (IS), transition state (TS) and the final state (FS) are shown. The solvation effect corrections were obtained by calculating the differences of the energies in the current solvation structures and the energies in the previous vacuum structures (Supporting Figure 15) for different states.

Free energy corrections for the initial, transition and final states of CO_2 exchange steps were calculated by considering the vibrational frequencies of the whole system in vacuum condition.

Correction results are listed in Supporting Table 1. A free energy barrier of 0.1941 eV is obtained for CO₂ exchange, which could be easily surmounted under electrochemical conditions.

Supporting Table 1: Solvation energy corrections (Sol Corr) and free energy corrections [including zero point energy (ZPE), enthalpy (H) and entropy (-TS) terms] for CO₂ exchange step (Supporting Figure 15). The corrections for IS, TS and FS were calculated. The units are in eV.

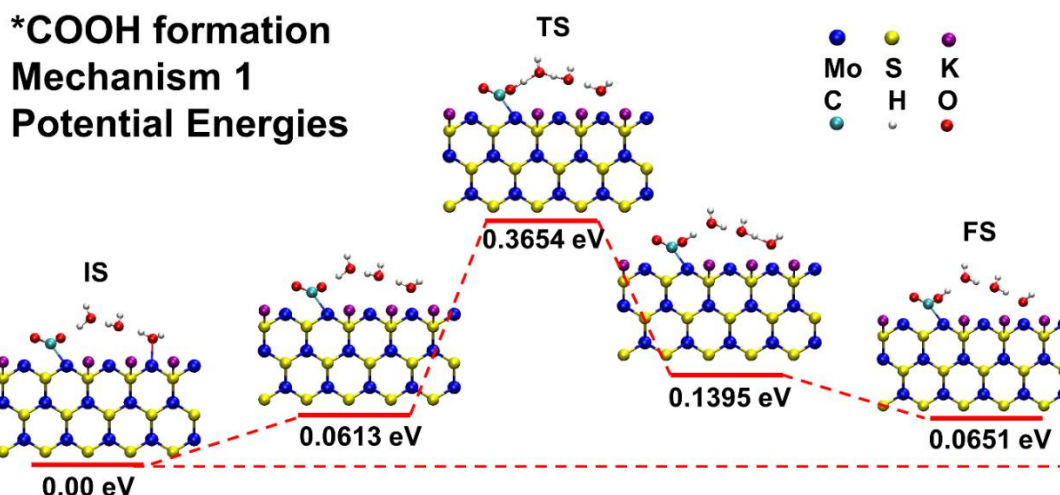
State	Sol Corr	ZPE	H	-TS	G-E _{elec}	Total Corr
IS	0.0000	1.6553	0.2390	-0.5431	1.3512	1.3512
TS	-0.0008	1.5778	0.2258	-0.5419	1.2617	1.2609
FS	0.0606	1.6432	0.2479	-0.6057	1.2854	1.3460

State	E _{elec}	Total Corr	G	G-G(IS)
IS	0.0000	1.3512	1.3512	0.0000
TS	0.2844	1.2609	1.5453	0.1941
FS	0.0007	1.3460	1.3467	-0.0045

S13.3. *COOH formation

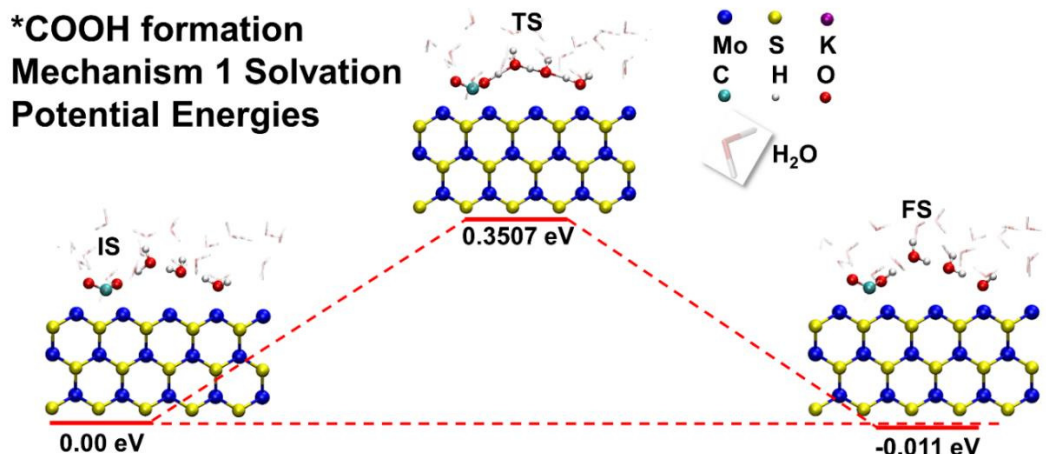
Supporting Figure 17 shows the complete potential energy landscape and corresponding atomic configurations for *COOH formation process with proton transport across 2 H₂O molecules. The initial state shows that *CO₂ is adsorbed on the MoS₂ surface with its C atom and one O atom attached to two neighboring Mo atoms, and the other O atom pointing outward, which is in a similar configuration with a previous study.^[18] One H₂O molecule residing near the Mo edges dissociates, with the help of the Mo atoms acting as a catalyst. The transition state configuration shows that the dissociated proton transports through the hydrogen bond network following the Grotthuss mechanism. A concerted fashion for proton transport is also revealed where all the 3 protons are equally shared by the host O atoms. The final state configuration shows one proton

finally approaches the $^*\text{CO}_2$ and gets bonded with its outward-pointing O atom to form the $^*\text{COOH}$ species. A potential energy barrier of 0.3654 eV is shown by the transition state.



Supporting Figure 17: Potential energy landscape of $^*\text{COOH}$ formation process through proton transport across two H_2O molecules. The initial state (IS), transition state (TS) and the final state (FS) are marked out.

Solvation effect corrections were calculated in a similar fashion as in Section S13.2. The MoS_2 surface was filled with 20 H_2O molecules surrounding the adsorbates. The structures of the solvating H_2O 's were relaxed with the original adsorbates kept fixed. Supporting Figure 18 shows the potential energy landscape with the corresponding solvated structures for the initial, transition and final states. The energy results again show the solvation effect corrections are small. This could be understood as H_2O molecules were explicitly involved in our transition state search, which could already account for a large portion of the solvation effect.



Supporting Figure 18: Potential Energy landscape of *COOH formation process through proton transport across two H₂O molecules, with explicit solvation. Only the initial state (IS), transition state (TS) and the final state (FS) are shown.

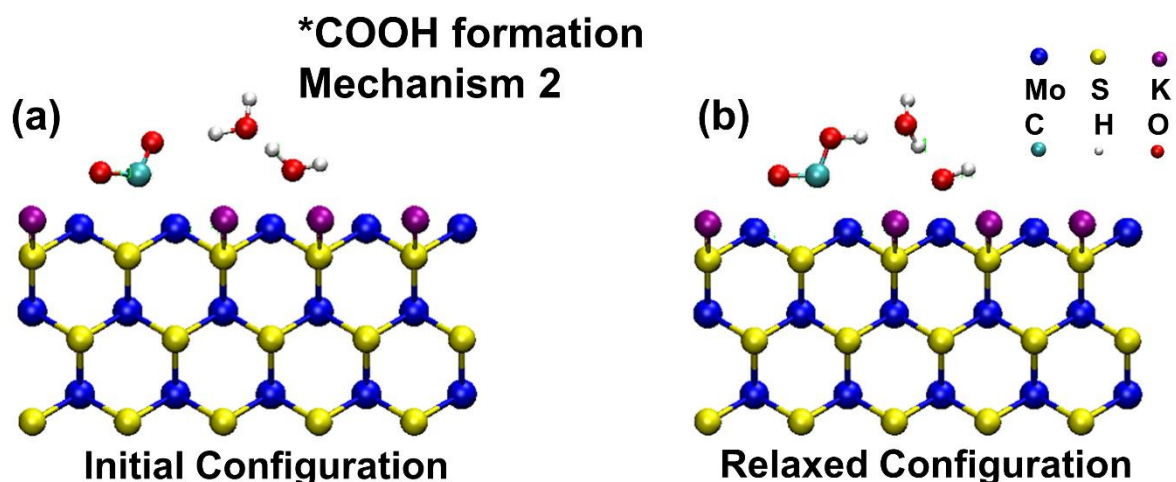
Free energy corrections for the initial, transition and final states were calculated with the vibrational frequencies of only the adsorbates in vacuum condition. The correction results are presented in Supporting Table 2, A free energy barrier of 0.2072 eV is shown for this specific *COOH formation mechanism.

Supporting Table 2: Solvation energy (Sol Corr) and free energy corrections [zero point energy (ZPE), enthalpy (H) and entropy (-TS) terms] for *COOH formation process through proton transport across 2 H₂O molecules (Supporting Figure 17). The corrections for IS, TS and FS were calculated. The units are in eV.

State	Sol Corr	ZPE	H	-TS	G-E _{elec}	Total Corr
IS	0.0000	2.2021	0.2613	-0.5062	1.9571	1.9571
TS	-0.0147	2.0182	0.2285	-0.4331	1.8136	1.7989
FS	-0.0761	2.2006	0.2763	-0.5138	1.9631	1.8870

State	E _{elec}	Total Corr	G	G-G(IS)
IS	0.0000	1.9571	1.9571	0.0000
TS	0.3654	1.7989	1.7989	0.2072
FS	0.0651	1.8870	1.8870	-0.0005

Another mechanism for *COOH formation was also explored in which *COOH was formed through proton transport across 1 H₂O molecule. The initial configuration of *CO₂ with 2 additional H₂O near the Mo edges was setup as shown in Supporting Figure 19a, acting as a starting point for the subsequent structural relaxations. During the structural optimization, we observed that the 2 H₂O molecules moved closer to the *CO₂ and proton transport occurs spontaneously to produce the *COOH species as shown in Supporting Figure 19b. These results show that *COOH adsorbate is energetically favorable under the current setup. Again, this confirms that the important intermediate *COOH could be easily obtained with H₂O providing proton with the help of MoS₂ catalyst.

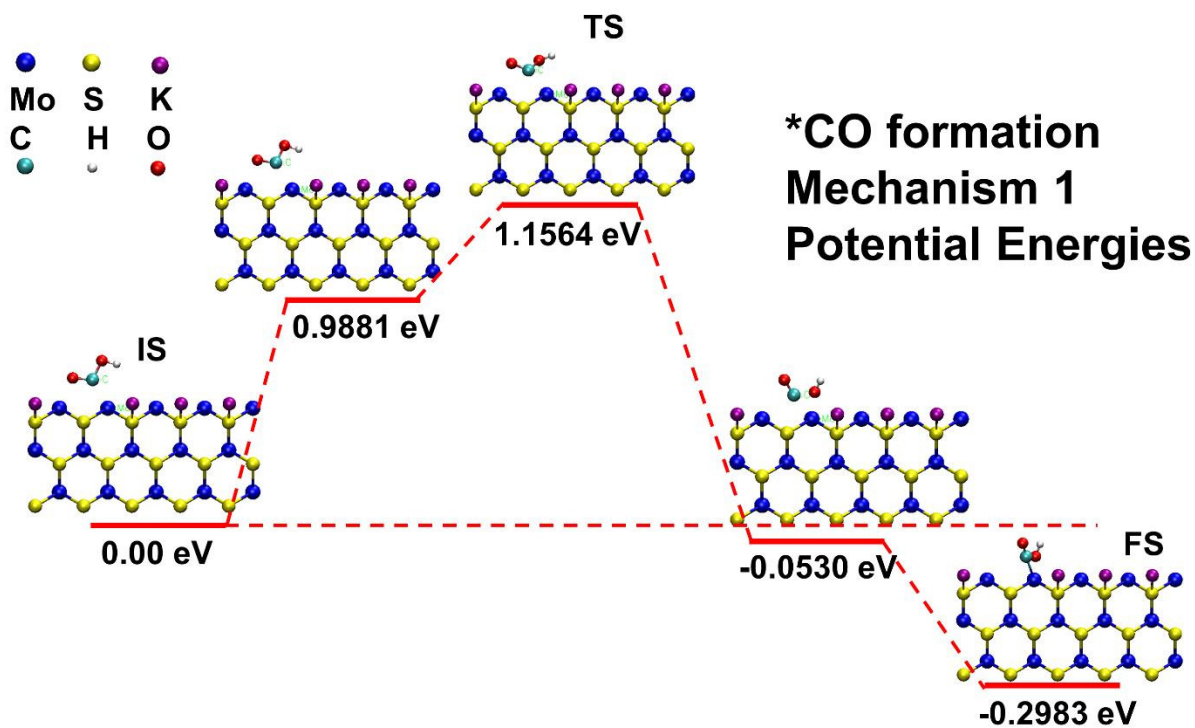


Supporting Figure 19: Structural relaxation directly shows *COOH formation through proton transport across one H₂O molecule. (a) The initial structure setup before relaxation. (b) The final configuration after relaxation, showing *COOH formation.

S13.4. *CO formation (*COOH C-OH bond breaking)

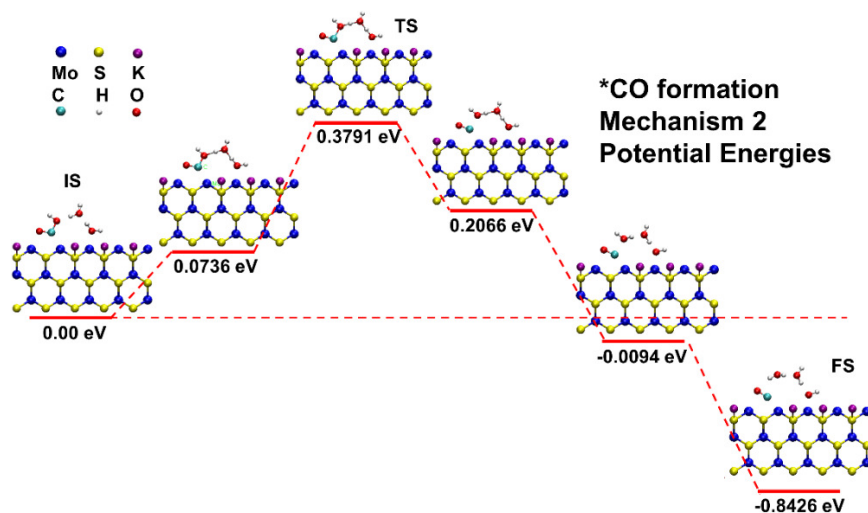
After the formation of *COOH, the C-OH bond breaks to produce *CO. Two mechanisms were explored for this. Supporting Figure 20 shows the mechanism of direct C-OH bond breaking with the help of MoS₂ catalyst. The transition state configuration shows the hydroxyl group

rotates and approaches the metal surface. A large potential energy barrier of 1.1564 eV is observed, which would prevent this process from occurring under room temperature.



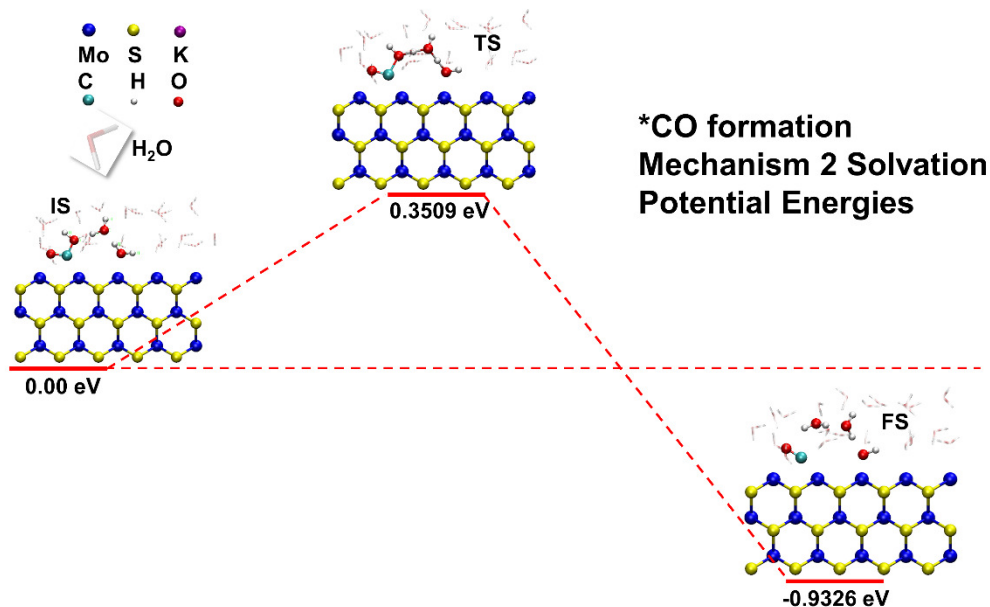
Supporting Figure 20: Potential energy landscape of *CO formation. The C-OH bond of the *COOH breaks directly catalyzed by MoS₂. The initial state (IS), transition state (TS) and the final state (FS) are shown.

Supporting Figure 21 shows an alternative mechanism for C-OH bond breaking with the help of proton transport. The initial state configuration shows that *COOH with its -OH group pointing outward, similar to the configuration of *CO₂ in Supporting Figure 17 and 18.



Supporting Figure 21: Potential energy landscape of *CO formation. The C-OH bond of the *COOH breaks with the help of proton transport. The initial state (IS), transition state (TS) and the final state (FS) are marked out.

The transition state configuration again shows a concerted fashion for proton transport. The dissociated proton from the H₂O molecule near the Mo edges migrates through the hydrogen bond to a nearby bridging H₂O molecule, and one proton of the bridging H₂O is donated to the O atom in the -OH group of *COOH. At the same time, the C-OH bond of the *COOH is elongated from 1.44 Å to 1.74 Å. In the final state, the C-OH bond breaks, and the *CO species is formed. The potential energy barrier is shown as 0.3791 eV, which is much lower than the case of direct C-OH bond breaking. Solvation effect corrections and free energy corrections for this mechanism were calculated with the same approaches in Section S13.3. During the solvation process 20 water molecules were added to the system followed by the structural relaxations similar to what has done in Section 13.3. The potential energy landscape with solvated configurations for the initial, transition and final states are shown in Supporting Figure 22. The correction results are presented in Supporting Table 3. Finally, a free energy barrier of 0.2133 eV is obtained.



Supporting Figure 22: Potential energy landscape of *CO formation. The C-OH bond of the *COOH breaks with the help of proton transport. Explicit solvation is added. Only the initial state (IS), transition state (TS) and the final state (FS) are shown.

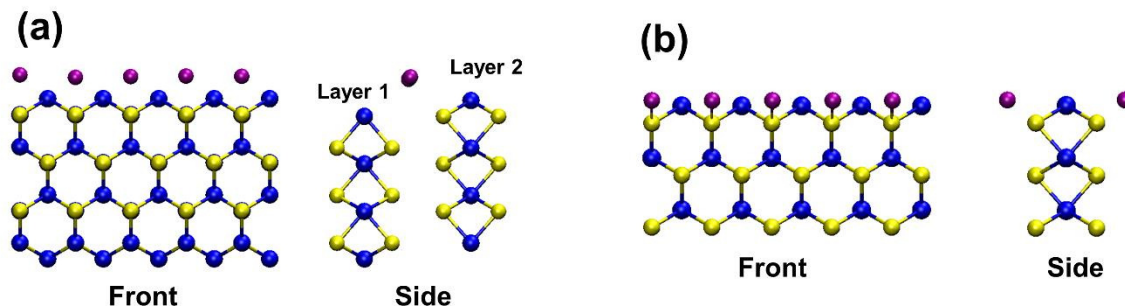
Supporting Table 3: Solvation energy (Sol Corr) and free energy corrections [zero point energy (ZPE), enthalpy (H) and entropy (-TS) terms] for *CO formation process with the help of proton transport (Supporting Figure 21). The corrections for IS, TS and FS were calculated. The units are in eV.

State	Sol Corr	ZPE	H	-TS	G-E _{elec}	Total Corr
IS	0.0000	1.8779	0.2280	-0.4485	1.6574	1.6574
TS	-0.0282	1.7200	0.2081	-0.4083	1.5198	1.4916
FS	-0.0900	1.8334	0.2511	-0.5421	1.5424	1.4524

State	E _{elec}	Total Corr	G	G-G(IS)
IS	0.0000	1.6574	1.6574	0.0000
TS	0.3791	1.4916	1.8707	0.2133
FS	-0.8426	1.4524	0.6098	-1.0476

S13.5. K binding to MoS₂ surface

The interactions between K atoms and MoS₂ surfaces were explored, and the relaxed structure is shown in Supporting Figure 23a. 2 layers of MoS₂ NFs with a stacked configuration were used. We see from the side view that K atoms are located between the two layers, and from the front view we see K atoms are located between the gaps of two neighboring Mo atoms of Layer 2 MoS₂ NF. In real cases, K's exist as K⁺ ions, and the MoS₂ surface acts as a cathode and is negatively charged. We expect the K's would stay closer to the MoS₂ surface (The classical molecular dynamics results reveal this point, see the density distribution shown in Figure 4b of the main text). In all our DFT calculations to explore MoS₂ catalytic properties, the systems of MoS₂ with adsorbed K's were constructed following the classical MD results, as shown in Supporting Figure 23b.

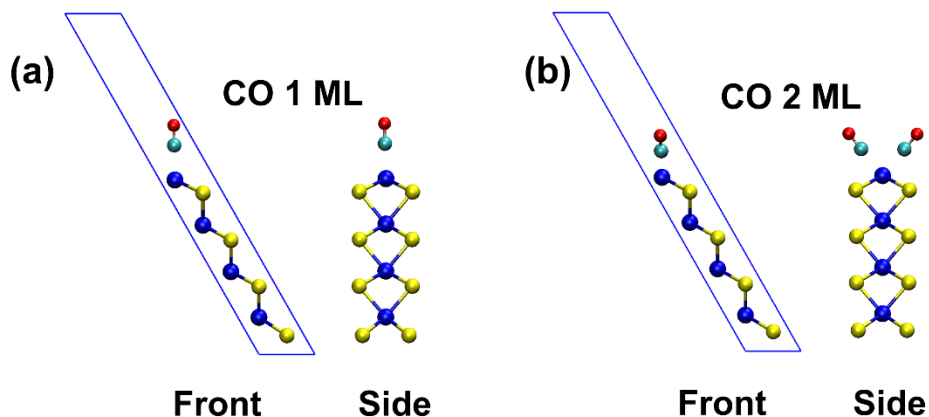


Supporting Figure 23: (a) Front and side views for the DFT-relaxed structure of K's residing between two MoS₂ layers. (b) Front and side views for the structure of K's binding to the MoS₂ monolayer, constructed following classical MD results (see Figure 4 in the main text). This structure was used to explore the MoS₂ catalytic properties.

S13.6. CO coverages and binding energies

The produced CO should be desorbed from the MoS₂ surface to facilitate the subsequent reduction reactions. We calculated the binding free energies between CO and MoS₂ to how difficult it is for CO to be released. MoS₂ monolayers (4 Mo atoms and 8 S atoms each) with zigzag Mo edges under periodic boundary conditions were used, with Gamma- centered 8×1×1

k-grids. Supporting Figure 24a shows the relaxed structures of CO binding to MoS₂ surface with 1 monolayer (ML) coverage where each Mo atom adsorbs one CO. Supporting Figure 24b shows the 2 ML case where each Mo atom adsorbs two CO's.



Supporting Figure 24: (a) Front and side views for the DFT-relaxed structure of one CO binding to one Mo atom. The coverage is 1 monolayer (ML). (b) Front and side views for the DFT-relaxed structure of two CO binding to one Mo atom. The coverage is 2 monolayer (ML).

The free energy corrections for the integrated systems (MoS₂ + CO's) were obtained by considering only the vibrational degrees of freedom of the CO adsorbates, same as the previous sections. However, when calculating the free energies of the isolated CO molecules, we considered all translational, rotational and vibrational degrees of freedoms. Since in our experiments, the overall Faradic efficiency is $90\% \pm 5\%$ (see Supporting Figure 5), we consider the Fugacity of CO to be 1 atm. The standard models (11) were used to calculate the free energy terms of an isolated CO molecule at 298 K temperature and 1 atm Fugacity. It should also be noted that when calculating the potential energy of an isolated CO molecule, a correction of -0.51 eV was added to our DFT output. This is due to the systematic errors introduced by using PBE exchange-correlation functional to describe the isolated molecules.^[19]

Supporting Table 4: Free energy corrections for the systems of CO binding to MoS₂ (1 ML and 2 ML coverages), isolated MoS₂ and isolated CO. The binding energies shown for 1 ML coverage is the average binding energy per CO molecule. For 2 ML coverage, the value is the average binding energy per second CO molecule. The units are in eV.

Structure	E _{elec}	ZPE	H	-TS	G-E _{elec}	G
MoS ₂ + CO (1 ML)	-99.1698	0.1913	0.0518	-0.1000	0.1431	-99.0267
MoS ₂ + CO (2 ML)	-115.3372	0.4167	0.1145	-0.2445	0.2868	-115.0504
MoS ₂	-82.4269	0	0	0	0	-82.4269
CO	-14.7962-0.51 = -15.3062	0.1369	0.1103	-0.6177	-0.3705	-15.6767

Structure	CO binding energy
MoS ₂ + CO (1 ML)	-0.9231
MoS ₂ + CO (2 ML)	-0.3470

The energy results are presented in Supporting Table 4. We observe that under 1 ML coverage the average binding energy per CO on Mo edges is -0.9231 eV. However, under the 2 ML coverage, the average binding energy per second CO is decreased to -0.3470 eV, which leads to easier desorption of the second CO. This suggests that during the reduction reactions, the Mo edges have a high CO coverage (> 1 ML).

S14. Classical molecular dynamics simulation (MD)

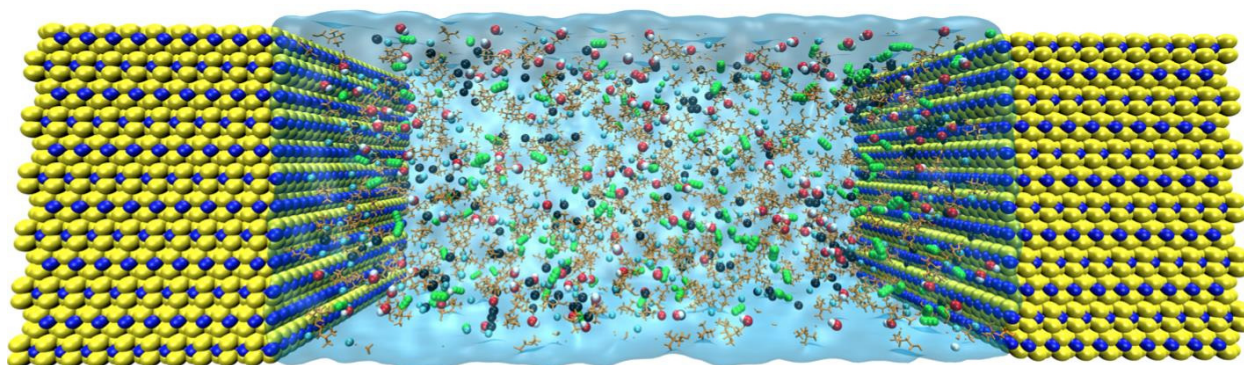
We performed classical MD simulations to study the diffusion of various species in bulk and their molecular arrangement close to the MoS₂ edges for different electrolytes considered in the experiments. Supporting Table 5 summarizes the electrolyte systems studied by classical MD simulations.

Supporting Table 5. Description of the systems simulated in this work.

System	Electrolyte (composition)
I	EMIMBF ₄ (50% vol)
II	Choline Chloride (0.5M)
III	Choline Chloride (2.0M)
IV	Choline Chloride/KOH (0.5M:1M)
V	Choline Chloride/KOH (1M:1M)

For the bulk electrolyte simulations, random configurations were initially equilibrated in the NVT ensemble by a simulated annealing procedure with the following sequential steps: melting at T=533.15 K for 1ns, annealing from 533.15 K to 298.15 K for 1ns, and equilibrating at 298.15 K for 1ns. Furthermore, the final configuration was equilibrated for 2ns followed by a production run of 10ns in the isothermal-isobaric ensemble (NPT) at the pressure of 1atm and temperature of 298.15 K. For the van der Waals (vdw) interactions, we used the standard 12-6 Lennard-Jones potential with a switch function and a cutoff length of 1.3 nm. The Coulomb interactions were treated via a combination of particle mesh Ewald summation^[20] and a switch function with a real space cutoff of 1.3 nm and FFT grid spacing of 0.1nm. Long range dispersion corrections for energy and pressure were applied during bulk MD simulations. The force field parameters for choline and chloride molecules were adopted from ref.^[21] For potassium and hydroxyl ions, we used the CHARMM22^[22] force field. The interaction parameters for CO₂ molecules were obtained from ref.^[23] and water molecules were modeled via the extended simple point charge (SPC/E) water model. During the simulations, all bonds were constrained. We used LINCS algorithm to keep all bonds rigid. Bulk density of each species is obtained from the NPT

simulations such that it corresponds to the experimental composition of the molecules in the electrolyte system. Supporting Table 6, summarizes the average bulk density, molar composition, and self-diffusion coefficient of all the species for different electrolyte systems mentioned in Supporting Table 5.



Supporting Figure 25. Schematic representation of MD simulation setup consists of two MoS₂ blocks on the left and right (blue and yellow), choline (orange), K⁺ (black), Cl⁻ (cyan), OH⁻ (red), CO₂ (green), and water (ice blue) molecules.

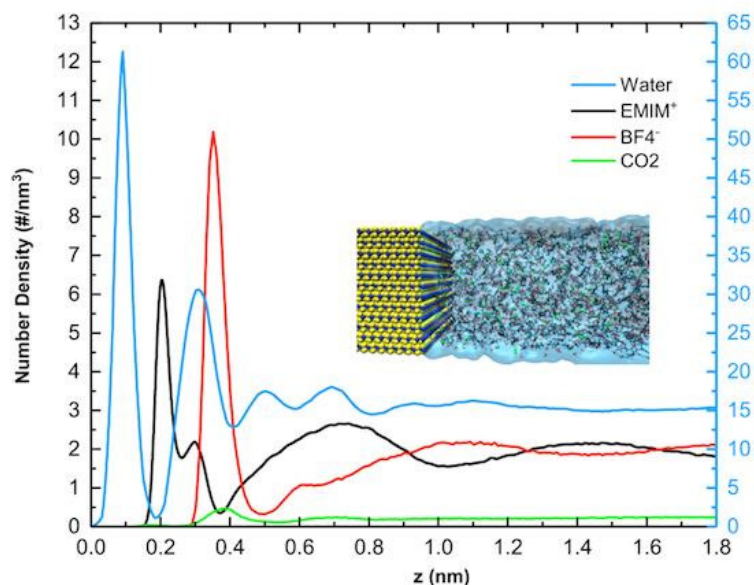
Supporting Figure 25, illustrates the schematic view of the simulation setup for the electrolyte system near the MoS₂ nanoflakes. The force field for the MoS₂ atoms was adopted from ref ^[24]. The Lorentz-Berthelot mixing rules were applied for all the non-bonded interactions, except for molybdenum- and sulfur-water interactions, which were modeled according to the force field parameters given in ref.^[25] In order to gain insight into the electric double layer (EDL) region close to the MoS₂ cathode, we adopted the constant charge approach to mimic the cathode in the experiments. Although specifying a constant charge on the wall is less realistic compared to the constant potential approach, it is at least an order of magnitude faster, and for planar geometries, it gives a fair description of the EDL structure at the surface of an electrode.^[26] Thus, we simulated the electrolytes close to the negatively charged MoS₂ wall (left wall located at $z = 0$, see Supporting Figure 25), with charge density of $\sigma_w = -0.053 \text{ e nm}^{-3}$. To compensate for this excessive negative charge, an equal amount of positive charge was located on the right wall to

maintain system charge neutrality. In other words, the channel shown in Supporting Figure 25 is actually a capacitor with electrodes made of MoS₂ of charge density of $\sigma_w = 0.053 \text{ e nm}^{-3}$. Note that there is a large enough distance of 17 nm between two electrodes to avoid the overlap of EDLs and ensure enough bulk-like region in the system. In each of the confined MD systems, the number of species was tuned so that the density in the channel center (where no oscillation of density is observed) matched that of bulk densities of NPT simulations given in Supporting Table 6. It should be noted that all the density distributions are measured relative to the position of the outermost Mo edge atom in the z direction.

Supporting Table 6. Bulk number density (nm^{-3}), composition, and self-diffusion coefficient (cm^2/s) of various species in different bulk electrolyte system.

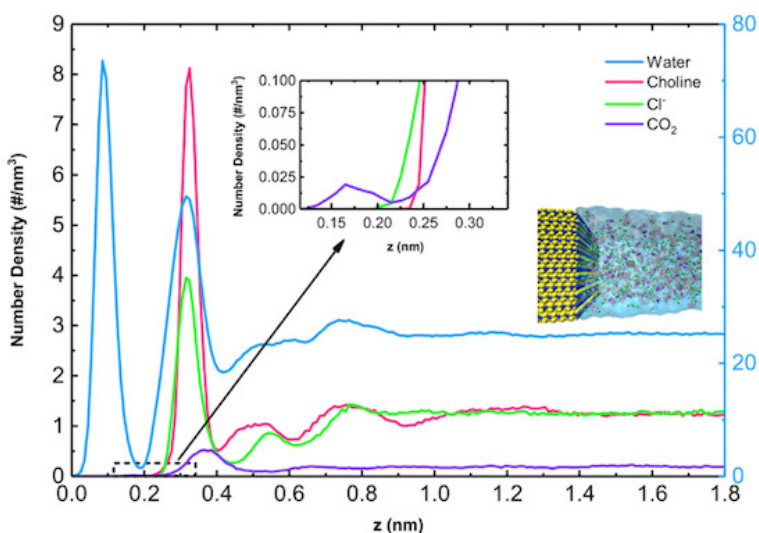
System	Species	Density	Composition	Diffusion ($\times 10^{-6}$)
(I)	EMIM	1.9432	50%	2.276 ± 0.149
	BF ₄	1.9432	50%	2.808 ± 0.181
	CO ₂	0.1918	0.3M	8.549 ± 0.470
	H ₂ O	16.610	Rest of the system	6.609 ± 0.099
(II)	Choline	0.2965	0.5M	7.951 ± 0.097
	Cl	0.2965	0.5M	12.512 ± 0.355
	CO ₂	0.1781	0.3M	18.689 ± 0.993
	H ₂ O	31.4183	Rest of the system	20.6 ± 0.715
(III)	Choline	1.2447	2.0M	3.288 ± 0.104
	Cl	1.2447	2.0M	5.781 ± 0.077
	CO ₂	0.1867	0.3M	9.616 ± 0.316
	H ₂ O	25.2169	Rest of the system	10.400 ± 0.228

(IV)	Choline	0.2985	0.5M	5.239±0.374
	Cl	0.2985	0.5M	10.077±0.197
	K	0.5970	1.0M	9.722±0.291
	OH	0.5970	1.0M	6.438±0.352
	CO ₂	0.1944	0.32M	16.955±0.050
	H ₂ O	31.63	Rest of the system	16.930±1.527
(V)	Choline	0.6387	1.0M	3.791±0.088
	Cl	0.6387	1.0M	7.742±0.267
	K	0.6387	1.0M	7.118±0.133
	OH	0.6387	1.0M	4.618±0.105
	CO ₂	0.1932	0.32M	12.358±0.050
	H ₂ O	29.3544	Rest of the system	13.262±0.346



Supporting Figure 26. Classical MD simulation results of the center of mass number density distribution of various molecules in 50% vol EMIMBF₄ electrolyte system close to the negatively charged MoS₂ wall with charge density of $\sigma_w = -0.053 \text{ e nm}^{-3}$. The zero on the z axis is set to the outermost Mo edge atom location.

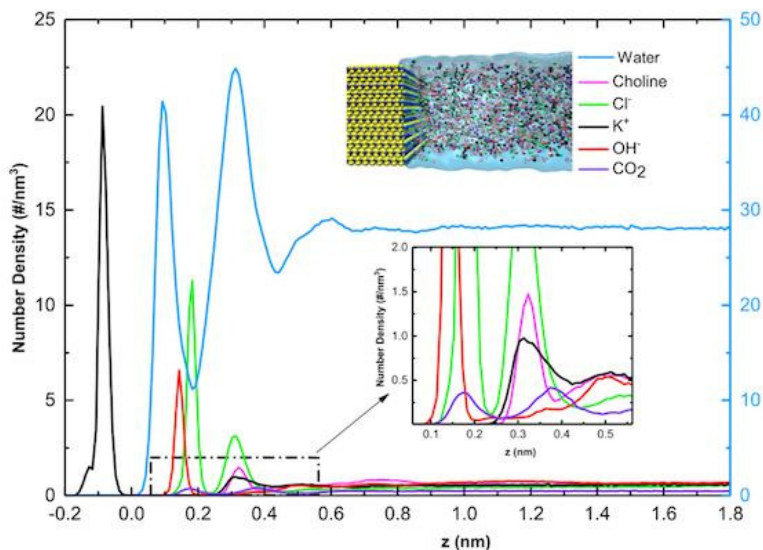
Supporting Figure 26 shows the EDL region in 50% vol EMIMBF₄ electrolyte system close to the negatively charged MoS₂ edges. As shown in the figure, when exposed to the negatively charged cathode, the EMIM⁺ ions are accumulated closer to the surface due to the electrostatic attraction, while the BF₄⁻ ions are repelled from the electrode. Furthermore, the CO₂ density profile exhibits a very small spike at ~1.7 Angstrom. This can be attributed to the large size and steric effect arising from the presence of EMIM cations close to the cathode surface, which in turn restricts the accessibility of CO₂ molecules to the active edge sites.



Supporting Figure 27. MD simulation results for the center of mass number density distribution of various molecules in choline chloride (2.0M) electrolyte system close to the negatively charged MoS₂ wall with charge density of $\sigma_w = -0.053 \text{ e nm}^{-3}$. Inset shows the zoomed-in region of CO₂ first density peak in the EDL close to the interface. The zero on the z axis is set to the outermost Mo edge atom location.

Supporting Figure 27 shows the number density profiles of various molecules in the EDL region of choline chloride (2.0M) electrolyte system close to the negatively charged MoS₂ edges. Although the surface is negatively charged, which results in the arrangement of choline cations close to the cathode surface, Cl⁻ ions are also capable of getting into the space among these larger-sized choline molecules (see the first density peak locations of choline and Cl molecules in Supporting Figure 27), which is because of their smaller size and favorable electrostatic

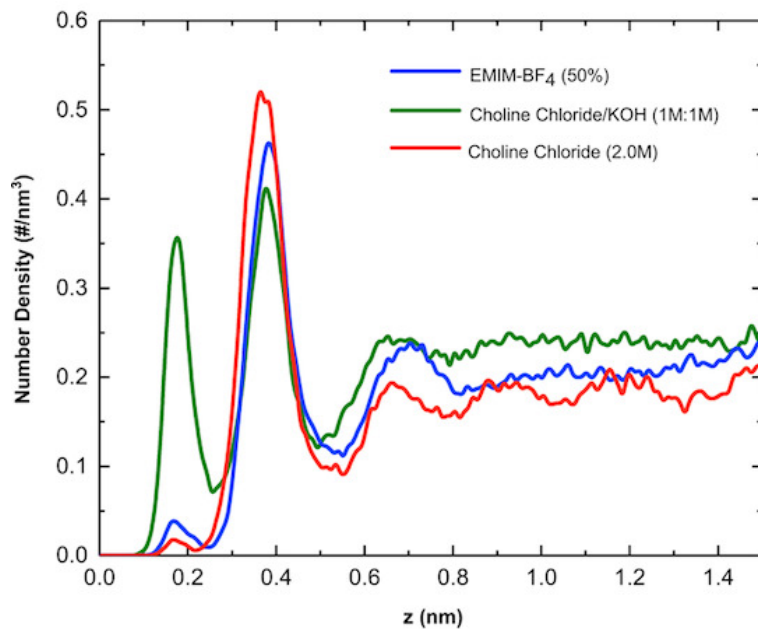
interactions between them and choline ions. Similar to the case of the EMIMBF₄ electrolyte system, the bulky choline molecules prevent accumulation of CO₂ molecules very close to the surface, which can affect their accessibility to the cathode active edge sites.



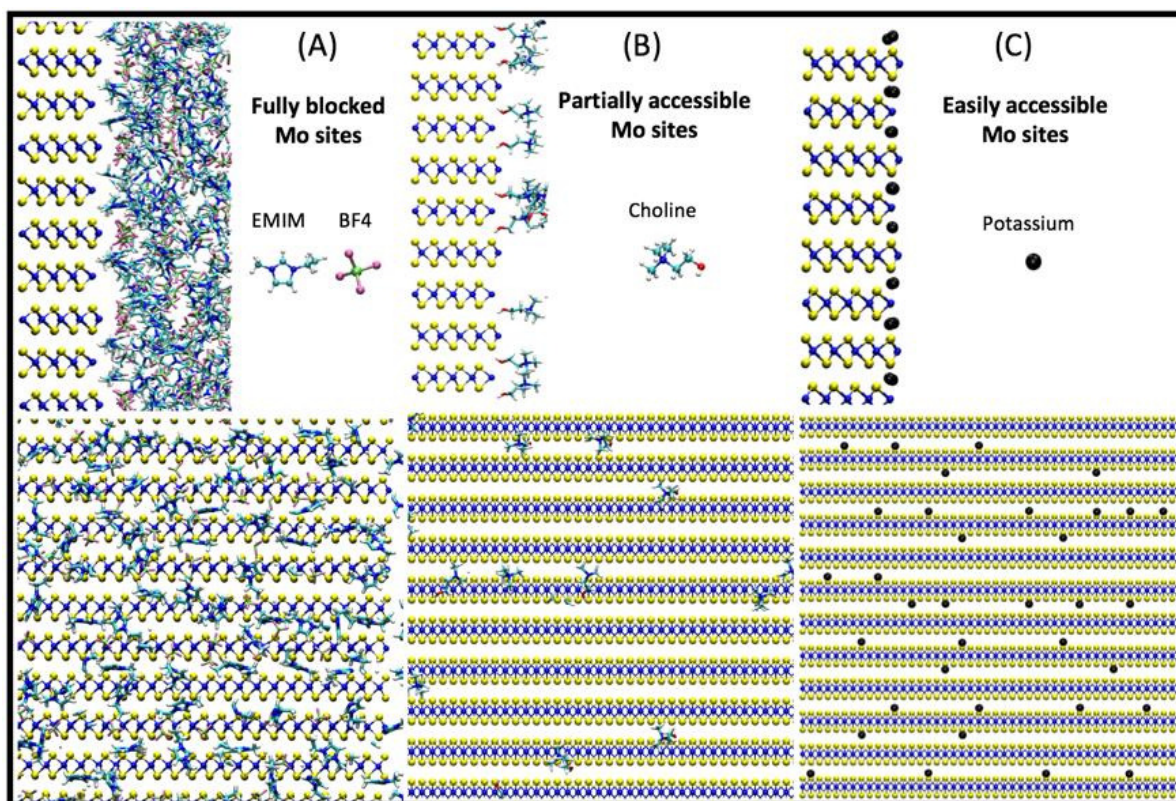
Supporting Figure 28. MD simulation results for the center of mass number density distribution of various molecules in choline chloride/KOH (1M:1M) electrolyte system close to the negatively charged MoS₂ wall with charge density of $\sigma_w = -0.053 \text{ e nm}^{-3}$. Inset shows the zoomed-in region of number density distributions in the EDL close to the interface. The zero on the z axis is set to the outermost Mo edge atom location.

Supporting Figure 28 shows the number density profiles of various molecules in the EDL region of choline chloride/ KOH (1M:1M) electrolyte system close to the negatively charged MoS₂ edges. In this system, the cathode surface exhibit strong propensity for the K⁺ adsorption over the choline molecules. Due to their smaller size and steric effects, K⁺ ions are easily accumulated near the MoS₂ edges, which produces higher peaks of K⁺ concentration than those of choline molecules. In addition, the high-density peak of K⁺ atoms causes a strong electrostatic attraction so that the first density peaks of Cl⁻ and OH⁻ ions are located very close to each other. A remarkable difference between electrolyte systems containing KOH versus choline chloride and EMIMBF₄ solutions is the CO₂ molecules first density peak. By adding KOH to the choline chloride electrolyte system, for the same composition, we observe a higher concentration of CO₂

molecules close to the cathode surface (See Supporting Figure 29). This can be attributed to the fact that, unlike the larger-size choline and EMIM molecules, K^+ atoms have smaller steric effects, that allows for more CO_2 molecules to be adsorbed near the cathode surface. In addition, big molecules such as choline and EMIM cover the Mo edges, while the smaller-size K^+ atoms can penetrate into the space between the edge Mo atoms (see Supporting Figure 29), exposing more available reaction sites for the CO_2 reduction. Thus, from classical MD simulations, we observe that for the EMIMBF₄ and choline chloride electrolyte systems, where the CO_2 first density peak is of the same order (see Supporting Figure 28), self-diffusion coefficient of the CO_2 molecules can be one of the influential factors for observing the higher experimental current density in the choline chloride solution. It can be seen that by adding KOH to the system, the first density peak of CO_2 molecules becomes almost 19 times higher compared to the choline chloride system. As a corollary, there are more CO_2 molecules to participate in the reduction process with the presence of KOH. This indicates that such a higher first density peak of CO_2 molecules can play an important role in the reduction process.



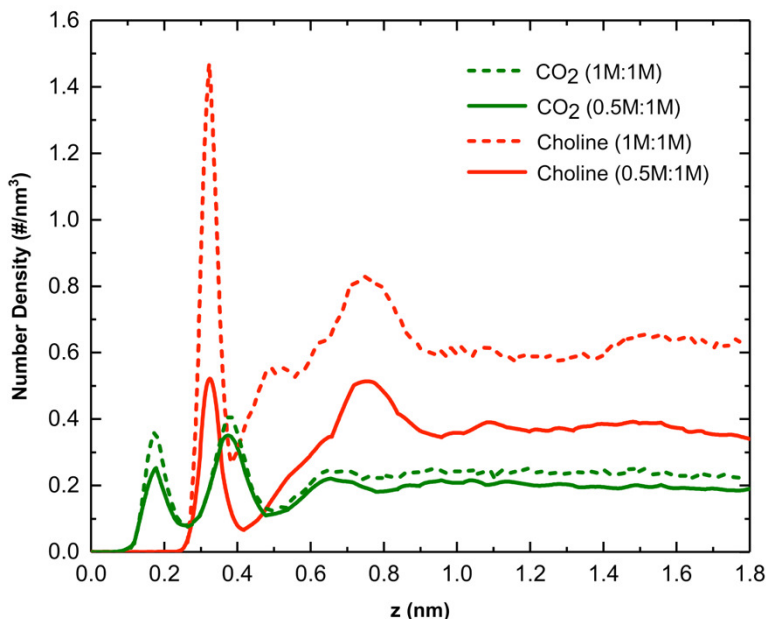
Supporting Figure 29. Comparison of CO₂ COM density layering in systems I, III, and V for wall charge density of $\sigma_w = -0.053 e nm^{-3}$.



Supporting Figure 30. MoS₂ edge coverage from side (top row) and top view (bottom row) in electrolyte systems I, II, and III: (A) Fully blocked Mo Sites by EMIM cations close to the surface. (B) Partially accessible Mo sites in choline chloride electrolyte system. (C) Easily accessible Mo sites in choline chloride/KOH electrolyte system.

To examine the effect of the molarity of choline chloride solution on the current density, the COM number density profiles of CO₂ and choline molecules near the negatively charged cathode surface are shown in Supporting Figure 31. It can be seen that in the 1M choline chloride solution, both CO₂ and choline density profiles are enhanced. It was shown by the DFT results,^[27] that the CO₂ molecules have a large interaction energy with components of choline chloride solution. This suggests that aqueous choline chloride solution acts as agents to capture CO₂ molecules. In Supporting Figure 31, it can be seen that an increase in the choline concentration, exposes more CO₂ molecules to MoS₂ NFs cathode for an equal wall charge density. Thus, the higher availability of CO₂ molecules to the reaction sites can increase the reduction performance. However, it should be noted that the increase in choline chloride content

can adversely affect the species transport from the bulk to the cathode surface (see Supporting Table 6). Therefore, there is a trade-off in increasing molarity of the choline chloride and diffusivity of reactants toward the cathode active edge sites.



Supporting Figure 31. Comparison of CO₂ and choline COM number density profile in electrolyte systems IV and V for wall charge density of $\sigma_w = -0.053 \text{ e nm}^{-3}$.

References:

- [1] J. Jiang, H. Li, L. Dai, H. Hu, C. Zhao, *AIP Adv.* **2016**, 6, 2.
- [2] M. Asadi, B. Kumar, C. Liu, P. Phillips, P. Yasaei, A. Behranginia, P. Zapol, R. F. Klie, L. A. Curtiss, A. Salehi-Khojin, *ACS Nano* **2016**, 10, 2167.
- [3] M. Asadi, K. Kim, C. Liu, A. V. Addepalli, P. Abbasi, P. Yasaei, P. Phillips, A. Behranginia, J. M. Cerrato, R. Haasch, P. Zapol, B. Kumar, R. F. Klie, J. Abiade, L. A. Curtiss, A. Salehi-Khojin, *Science (80-.)*. **2016**, 353, 467.
- [4] V. Sense, *Cell* **1990**, 35, 1.
- [5] S.-M. Park, J.-S. Yoo, *Anal. Chem.* **2003**, 75, 455 A.
- [6] B. A. Rosen, A. Salehi-Khojin, M. R. Thorson, W. Zhu, D. T. Whipple, P. J. Kenis, R. I. Masel, *Science (80-.)*. **2011**, 334, 643.
- [7] Z. S. Othman, N. H. Hassan, S. I. Zubairi, *J. Chem.* **2017**, 2017, DOI

10.1155/2017/9434168.

- [8] M. E. Merritt, C. Harrison, C. Storey, F. M. Jeffrey, A. D. Sherry, C. R. Malloy, *Proc. Natl. Acad. Sci.* **2007**, 104, 19773.
- [9] S. Verma, X. Lu, S. Ma, R. I. Masel, P. J. A. Kenis, *Phys. Chem. Chem. Phys.* **2016**, 18, 7075.
- [10] G. Henkelman, H. Jónsson, *J. Chem. Phys.* **2000**, 113, 9978.
- [11] G. Henkelman, B. P. Uberuaga, H. Jónsson, *J. Chem. Phys.* **2000**, 113, 9901.
- [12] C. J. Cramer, *Essentials of Computational Chemistry Theories and Models*, Wiley, **2004**.
- [13] M. Dunwell, Q. Lu, J. M. Heyes, J. Rosen, J. G. Chen, Y. Yan, F. Jiao, B. Xu, *J. Am. Chem. Soc.* **2017**, 139, 3774.
- [14] G. Henkelman, A. Arnaldsson, H. Jónsson, *Comput. Mater. Sci.* **2006**, 36, 354.
- [15] E. Sanville, S. D. Kenny, R. Smith, G. Henkelman, *J. Comput. Chem.* **2007**, 28, 899.
- [16] W. Tang, E. Sanville, G. Henkelman, *J. Phys. Condens. Matter* **2009**, 21, 084204.
- [17] M. Yu, D. R. Trinkle, *J. Chem. Phys.* **2011**, 134, 064111.
- [18] T. Sheng, S.-G. Sun, *Chem. Commun.* **2017**, 53, 2594.
- [19] A. A. Peterson, F. Abild-Pedersen, F. Studt, J. Rossmeisl, J. K. Nørskov, *Energy Environ. Sci.* **2010**, 3, 1311.
- [20] U. Essmann, L. Perera, M. L. Berkowitz, T. Darden, H. Lee, L. G. Pedersen, *J. Chem. Phys.* **1995**, 103, 8577.
- [21] D. C. McCalman, L. Sun, Y. Zhang, J. F. Brennecke, E. J. Maginn, W. F. Schneider, *J. Phys. Chem. B* **2015**, 119, 6018.
- [22] A. D. MacKerell, D. Bashford, M. Bellott, R. L. Dunbrack, J. D. Evanseck, M. J. Field, S. Fischer, J. Gao, H. Guo, S. Ha, D. Joseph-McCarthy, L. Kuchnir, K. Kuczera, F. T. K. Lau, C. Mattos, S. Michnick, T. Ngo, D. T. Nguyen, B. Prodhom, W. E. Reiher, B. Roux, M. Schlenkrich, J. C. Smith, R. Stote, J. Straub, M. Watanabe, J. Wiórkiewicz-Kuczera, D. Yin, M. Karplus, *J. Phys. Chem. B* **1998**, 102, 3586.
- [23] Z. Zhang, Z. Duan, *J. Chem. Phys.* **2005**, 122, 214507.
- [24] T. Liang, S. R. Phillpot, S. B. Sinnott, *Phys. Rev. B - Condens. Matter Mater. Phys.* **2009**, 79, 245110.
- [25] M. Heiranian, Y. Wu, N. R. Aluru, *J. Chem. Phys.* **2017**, 147, 104706.

- [26] C. Merlet, M. Salanne, B. Rotenberg, *J. Phys. Chem. C* **2012**, 116, 7687.
- [27] T. Altamash, M. Atilhan, A. Aliyan, R. Ullah, G. García, S. Aparicio, M. Tariq, S. Aparicio, A. R. Katritzky, R. D. Rogers, D. Nath, D. Gelowitz, W. Srisang, C. Saiwari, A. Benamor, M. Al-Marri, H. Shi, T. Supap, C. Chan, Q. Zhou, M. Abu-Zahra, M. Wilson, W. Olson, R. Idem, P. Tontiwachuthikul, *RSC Adv.* **2016**, 6, 109201.